06

Influence of Synthesis Conditions on the Structural, Optical, and Electrophysical Properties of TiO_2/Cu_xO Nanocomposites

© M.N. Martyshov,[1] A.V. Pavlikov,[1,2] E.V. Kytina,[1] O.V. Pinchuk,[2] T.P. Savchuk,[1,2] E.A. Konstantinova,[1] V.B. Zaitsev,[1] P.K. Kashkarov[1,3]

[1] Department of Physics, Moscow State University,
119991 Moscow, Russia
[2] National Research University of Electronic Technology – MIET,
124498 Zelenograd, Moscow, Russia
[3] National Research Center „Kurchatov Institute“,
123182 Moscow, Russia
e-mail: pavlikov@physics.msu.ru

Received September 8, 2022
Revised December 1, 2022
Accepted December 6, 2022

Nanocomposites based on anodic titanium oxide nanotubes with copper oxide nanoparticles were formed and their structural, optical, and electrophysical properties were studied. Defects in the structure of the samples were identified by electron paramagnetic resonance and it was shown that, as a result of copper oxide deposition, CuO nanoparticles were formed on the surface of nanotubes. It was found that the conductivity of the structure decreases by several orders of magnitude with an increase in the number of deposition cycles. It was shown that this effect could be associated with the formation of TiO_2/CuO heterojunctions on the nanotube surface. It was shown for the first time that an increase in the content of copper oxide in TiO_2/Cu_xO nanocomposites was accompanied by a decrease in conductivity and an increase in the number of defects.

Keywords: titanium oxide, nanotubes, nanocomposites, copper oxide nanoparticles, defects, conductivity.

DOI: 10.21883/TP.2023.02.55478.221-22n

Introduction

Photocatalytic materials based on nanostructured titanium dioxide (TiO_2) attract the researchers' attention due to their high chemical stability and photocorrosion resistance [1,2]. These materials have a large specific surface area and can be used for photocatalytic decomposition of organic impurities in air or water, and conversion of carbon dioxide (CO_2) to hydrocarbon fuels in the process of photocatalysis. Among the morphological varieties of TiO_2 nanostructures, nanotube arrays obtained by anodic oxidation [3] can be highlighted. Ordered arrays of nanotubular anodic titanium oxide (NTATO) can exhibit better diffusion of photocatalytic reaction products and lower recombination rate of photoinduced charge carriers compared to TiO_2 nanoparticles [4–6]. Currently, single-walled (SW) and multi-walled (MW) TiO_2 nanotubes are widely studied. In particular, it was shown that MW nanotubes have better photocatalytic activity in CO_2 conversion reactions compared to SW [7], but the efficiency of such materials as photocatalysts is still insufficiently high. Various additives, including nanoparticles of other semiconductor materials, are used to improve the photocatalytic properties of nanostructures based on TiO_2. It is known that TiO_2 is a high-energy-gap semiconductor ($E_g \sim 3.2\,\text{eV}$) and is not sensitive to visible light. This problem can be solved, for example, by doping TiO_2 with various impurities, both metals and non-metals, and also by adding particles of such low-energy-gap semiconductors as CdS, CdSe, V_2O_5 [8]. The introduction of impurities into TiO_2 is accompanied by the formation of energy levels in the forbidden band and, accordingly, by the expansion of the absorption spectrum into the visible region [8]. We developed a new original method for determining the position of the energy levels of impurity sites (defects) in the forbidden band of nanostructured semiconductors using electron paramagnetic resonance spectroscopy [9,10]. The combination of TiO_2 with low-energy-gap semiconductors also leads to the visible light absorption with subsequent injection of electrons into the conduction band of TiO_2, which ensures its photocatalytic activity. Another way to improve the photocatalytic properties of TiO_2 is to add *p*-type semiconductor particles [11–13]. As a result, $p-n$-heterojunctions are formed in the structure, since TiO_2 is *n*-type semiconductor [14]. An electric field arises in the $p-n$-junction region, which promotes the separation of photoinduced charges and, accordingly, delays the undesirable recombination of electrons and holes [15]. Copper oxide (CuO) has *p*-type conductivity and a forbidden band width $E_g = 1.7\,\text{eV}$ [16], and, therefore, is a promising material for modifying the photocatalytic properties of nanostructures based on TiO $_2$. Therefore, the aim of this paper was to synthesize arrays of MW nanotubes of anodic titanium oxide (MW-NTATO) modified with copper oxide nanoparticles and to compare their structural and optical properties, defect states, and charge carrier transport. Such

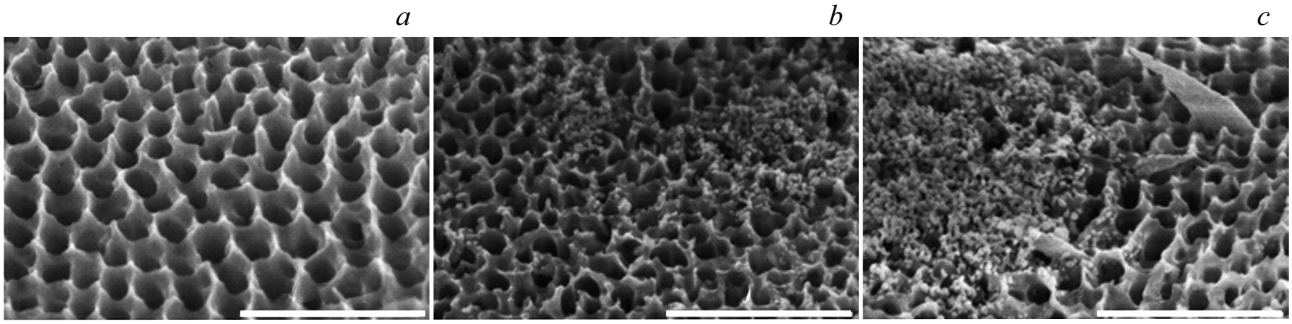

Figure 1. SEM image of the surface of the initial sample of MW-NTATO (*a*) and after ion deposition of copper oxide MW-NTATO/Cu_xO-30 (*b*), MW-NTATO/Cu_xO-60 (*c*).

sample characterization is necessary for further successful study of their photocatalytic properties.

1. Experiment procedure

The synthesis of TiO_2 MW nanotubes is described in detail in paper [7]. Copper oxide Cu_xO was deposited onto the surface of the MW-NTATO arrays using the Successive Ionic Layer Adsorbtion and Reaction — SILAR method. The source of copper ions was an aqueous solution of $CuCl_2 \cdot 2H_2O$, the pH of which was adjusted to 10 with a solution of 25% ammonia (NH_4OH). A solution of ethyl alcohol heated to 70°C with deionized water in a ratio of 1 : 3 was used as an anion source. The SILAR method consists of three stages. At the first stage, the sample is immersed for 30 s in the aqueous solution of copper chloride containing $[Cu(NH_3)_4]^{+2}$ ions. At the second stage the sample is immersed for 7 s in solution of ethyl alcohol with deionized water. At the third stage, the sample is washed for 30 s in deionized water. The amount of Cu_xO copper oxide deposited on MW-NTATO was varied by varying the number of ion deposition cycles — 10, 30, and 60 monolayers (MW-NTATO/Cu_xO-10, MW-NTATO/Cu_xO-30, MW-NTATO/Cu_xO-60, respectively). After successive ion layer absorption and reaction, the resulting structures were subjected to heat treatment in air at a temperature of 300°C for 60 min at a heating rate of 30° C/min.

The morphology of the samples was studied using a Helios NanoLab 650 Dual Beam microscope (FEI, the Netherlands). The studies were carried out at an accelerating voltage of 1 kV. Raman spectra were recorded on Horiba HR800 micro-Raman unit in backscattering geometry using a 10x lens. The excitation source was a helium-neon ($\lambda = 633$ nm) laser. The laser power was $W = 10$ mW. The use of diffraction grating 1800 lines/mm provided a spectral resolution of 1 cm^{-1}. The diffuse reflection spectra of the studied samples were recorded using LS-55 Perkin Elmer spectrometer. The design features of the spectrometer and the capabilities of the control software make it possible to record diffuse reflection spectra in the range of 200−800 nm with high accuracy at various angles of incidence of the probing beam on the surface. Electron paramagnetic resonance (EPR) spectra were recorded on Bruker ELEXSYS-E500 spectrometer (X-band, sensitivity 10^{10} spin/G). The concentration of paramagnetic sites (defects) was calculated using a standard ($CuCl_2 \cdot 2H_2O$ single crystal with a known number of paramagnetic sites). The g-factor values were determined using $MgO(Mn^{++})$ standard. Conductivity was measured using Keithley 6487 picoammeter. Voltage was applied to the sample from a source built into the picoammeter. ARS DE-204SE closed-cycle helium cryostat was used to monitor the temperature. Before measurements the samples were annealed at temperature of $T = 400$ K in vacuum for one and a half hours to stabilize the properties. Conductivity measurements were performed in the temperature range 240−400 K at pressure $p = 10$ mbar. Specific conductivity σ was calculated by the formula

$$\sigma = \frac{d}{S} \times \frac{1}{R},$$

where R — the value of the structure resistance obtained in the experiment, S — the area of the upper electrode, d — the thickness of the NTATO layer.

2. Experimental results

Fig. 1 shows SEM images of both the initial MW-NTATO samples and those with deposited copper oxide nanoparticles. The SEM results show that with increase in the number of deposition cycles, the size of deposited Cu_xO nanoparticles on the MW-NTATO surface increases. It is also noticeable that the deposition under such conditions leads to the formation of islands and uneven coverage of the NTATO array surface with nanoparticles. The average size of deposited copper oxide nanoparticles for MW-NTATO/Cu_xO-10/30/60 samples was 15, 22, and 20 nm, respectively. With increase in the number of deposition cycles, Cu_xO nanoparticles form agglomerates (stick together). At the same time, the average size of these nanoparticles remains approximately the same and

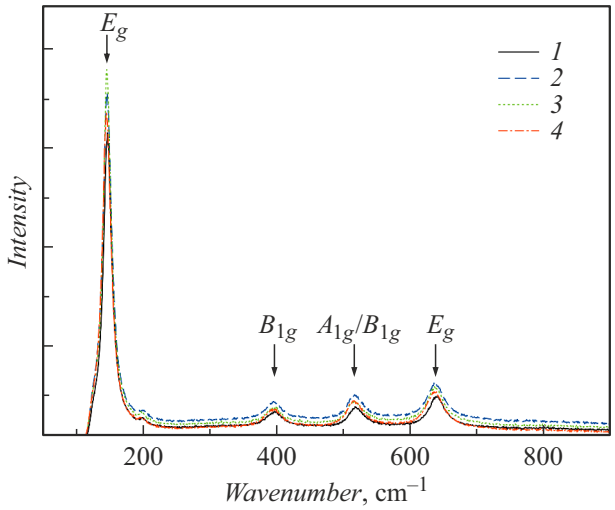

Figure 2. Raman spectra of initial samples MW-NTATO (*1*) and nanocomposites MW-NTATO/Cu_xO-10 (*2*), MS-NTAO/Cu_xO-30 (*3*), MW-NTATO/Cu_xO-60 (*4*).

does not depend on the number of cycles. A characteristic feature of MW-NTATO/Cu_xO-60 samples is the presence of copper oxide nanoparticles in the form of needles or sheets (Fig. 1, *c*).

Fig. 2 shows the Raman spectra of the initial MW-NTATO and MT-NTATO samples after 10, 30, and 60 cycles of copper oxide deposition. Spectral bands at 142 cm^{-1} (E_{1g}), 394 cm^{-1} (B_{1g}), 515 cm^{-1} (A_{1g}/B_{1g}) and 635 cm^{-1} (E_g) indicate the crystal structure of anatase [17]. The spectra of samples with deposited copper oxide layers contain the same lines as the original sample. This indicates that porous TiO_2 has a higher scattering efficiency than Cu_xO nanoparticles. According to literature data [18], signals in the Raman spectrum from copper oxides can be observed at 109–110, 146–153, 215, 300, 350, 515 and 638–665 cm^{-1}. The first three spectral lines and broad bands in the region of 500–550 and 638–665 cm^{-1} are characteristic for Cu_2O, while lines 300, 350 and 640 cm^{-1} are characteristic for CuO oxide. But the intensity of the lines in the Raman spectrum from thin oxide layers is much less than from titanium dioxide nanotubes. Moreover, the lines in the intervals 109–215, 370–420, 490–550, and 600–670 cm^{-1} are overlapped by intense MW-NTATO lines. This may be the reason why there are no noticeable changes in the Raman spectra in the Figure for MW-NTATO/Cu_xO compared to the initial sample.

Along with the structural properties, it is important to determine the band gap width, the absorption coefficient, including the contribution of the impurity absorption of the samples under study. These characteristics of the samples were obtained from the diffuse reflection spectra of light, since all samples are opaque and represent arrays of nanotubes on the surface of titanium foil. In particular, the spectral dependence of the absorption coefficient was determined from the diffuse reflection spectra of light. Before studying these spectra, we first studied the dependence of the scattering intensity on the angle of incidence of the probing radiation. It turned out that when the angle of incidence varied from 20 to 80°, the intensity of the scattered radiation practically did not change. For further measurements, the angle of incidence was 60°.

The characteristic shape of the diffuse reflection spectrum of light from MW-NTATO films is shown in Fig. 3, *a*. Diffuse scattering spectra of light make it possible to determine the value of the optical width of forbidden band E_g of semiconductor nanomaterials from the so-called intrinsic absorption edge. Despite the fact that there is no exact theory of multiple scattering, the theory of diffuse reflection and transmission of optically opaque samples is widely used — the so-called Kubelka and Munk two-component theory (see, for example, [19,20]). This theory assumes that the reflected radiation is isotropic, i.e. independent of direction, and the irradiating light is monochromatic. As a result of solving the system of Kubelka–Munk equations, it turns out that the diffuse reflection R_∞ of the sample depends only on the ratio of the absorption coefficient α

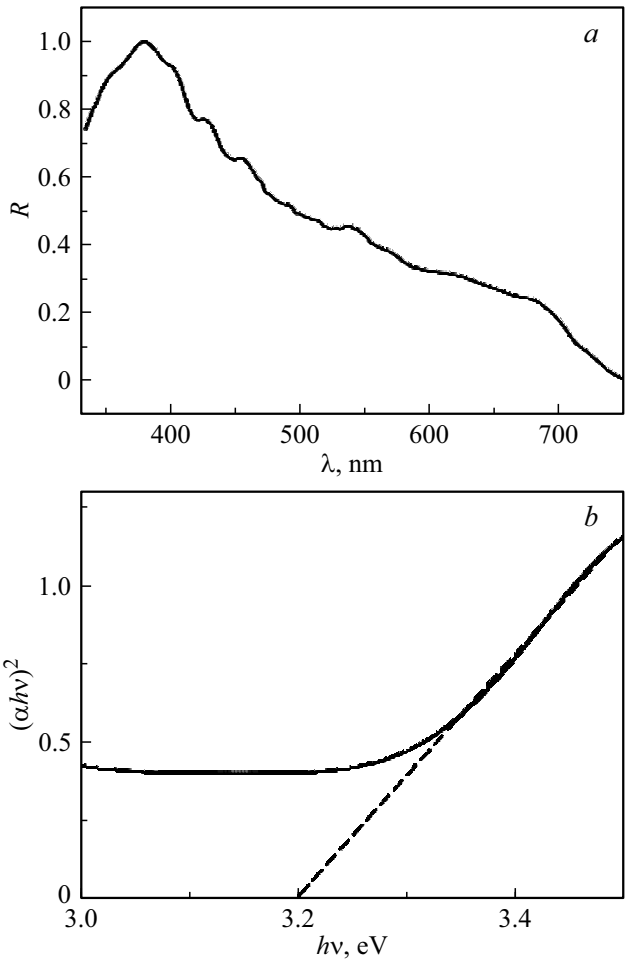

Figure 3. Normalized diffuse reflection spectrum of light from the MW-NTATO sample (*a*). Scheme for determining the forbidden band width according to the Kubelka–Munk theory for MW-NTATO (*b*).

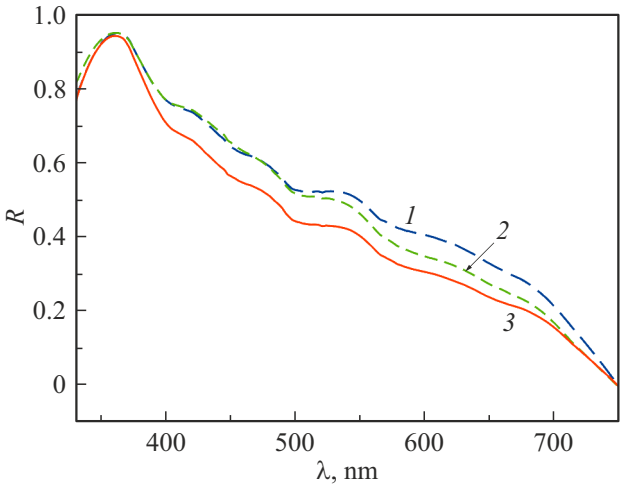

Figure 4. Normalized diffuse reflection spectra of nanocomposites MW-NTATO/Cu_xO-10 (*1*), MW-NTATO/Cu_xO-30 (*2*) and MW-NTATO/Cu_xO-60 (*3*).

and the scattering coefficient S, but not separately on the scattering coefficient or absorption coefficient:

$$\frac{\alpha}{S} = \frac{(1-R_\infty)^2}{2R_\infty} = F(R_\infty).$$

The function $F(R_\infty)$ is called the Kubelka–Munk function.

To determine the absorption coefficient $\alpha(\lambda)$ in a wide range of wavelengths it is necessary to obtain the dependence $S(\lambda)$. However, in practice, when determining the forbidden band width, it is always considered that the wavelength range in which the linear approximation of the dependence $\alpha(\lambda)$ is performed, is narrow enough (in our case — 20 nm) to consider S as constant in this range [19,20].

For the practical determination of the forbidden band width in the case of direct interband transitions the experimental data are presented in the form of the dependence

$$(\alpha\hbar\omega)^2 = A^2(\hbar\omega - E_g).$$

When analyzing MW-NTATO samples, the approach for indirect-gap semiconductors should be used. However, it was repeatedly shown that the application of the approach developed for semiconductors with direct interband transitions gives results that coincide, up to the measurement error, with the results for indirect-gap materials. This can be explained by the fact that, due to the size effect, the structure of the crystal lattice changes somewhat, which can lead to increase in the probability of direct interband transitions [21].

The graphical results of the analysis of diffuse reflection using the Kubelka–Munk theory are shown in Fig. 3, *b*. According to the performed calculations, the value of the forbidden band width for the MW-NTATO samples is 3.2 ± 0.1 eV. After the copper oxide introduction into the samples the diffuse reflection spectra of light depend on the amount of copper oxide — the corresponding results for MW-NTATO/Cu_xO are shown in Fig. 4. It can be seen from the Figure that the MW-NTATO/Cu_xO-60 samples have the highest light absorption in the visible region. Using the method described above, the values of the optical width of forbidden band were determined for the samples MW-NTATO/Cu_xO-10, MW-NTATO/Cu_xO-30 and MW-NTATO/Cu_xO-60. These values coincided within the error and amounted to 3.3 ± 0.1 eV. The amount of copper oxide on the surface of titanium dioxide nanostructures is so small that it cannot significantly affect the absorption of radiation.

Before proceeding to the analysis of charge carriers transport, it is necessary to study the nature and properties of defects in the structures under study. One of the sensitive methods for detecting defects, including copper ions, is EPR spectroscopy. Fig. 5 shows the results of the study by this method. In the EPR spectrum of the initial TiO_2 samples, the signal from dangling carbon bonds (C·) dominates, Land g-factor is $g = 2.0027$ [20]. The carbon presence in the composition of the samples is probably due to the ethylene glycol presence in the electrolyte and is also confirmed by elemental analysis data. The EPR spectra of the TiO_2/Cu_xO nanocomposites are a superposition of several EPR signals. First, a powerful EPR signal from copper ions Cu^{2+} ($g = 2.1612$) [22] is recorded, which indicates the presence of the CuO phase. In the left part of the EPR spectrum from copper ions, there is a „branch“ (denoted in Fig. 5 by *). This „branch“ may be due to an prohibited signal from copper ions Cu^{2+} replacing titanium ions in the TiO_2 lattice. Since titanium in the titanium dioxide lattice is in Ti^{4+} state, when it is replaced by copper ions Cu^{2+}, the formation of oxygen vacancies will occur. We do not observe them in the EPR spectrum, so we can conclude that they are nonparamagnetic. Also in the right part of the EPR spectrum (Fig. 5) there is a

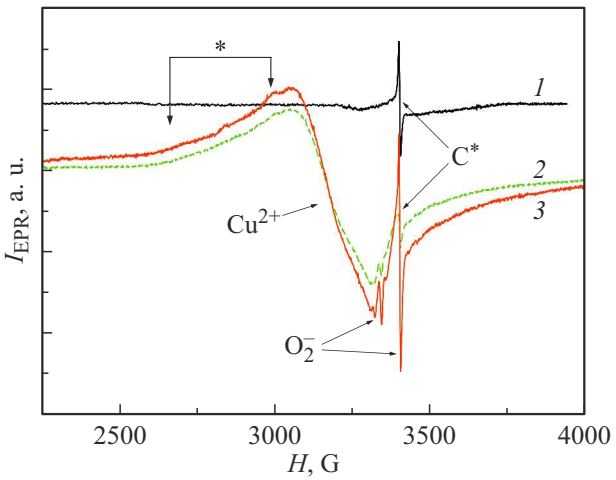

Figure 5. EPR spectra of the initial MW-NTATO (*1*) sample and MT-NTATO nanocomposites after 30 (*2*) and 60 (*3*) cycles of oxide deposition copper.

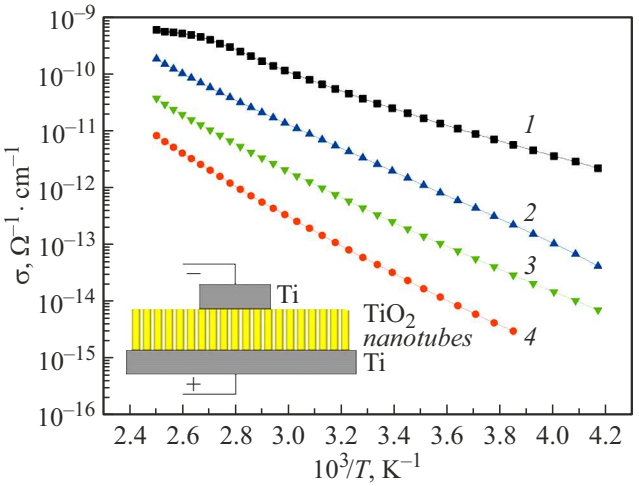

Figure 6. Temperature dependences of the specific conductivity of the initial sample MW-NTATO (*1*) and nanocomposites MW-NTATO/Cu_xO-10 (*2*), MS-NTAO /Cu_xO-30 (*3*) and MW-NTATO/Cu_xO-60 (*4*). On the insert — a schematic view of the structure used to measure the conductivity.

Specific conductivity of samples at room temperature and conductivity activation energies

Sample	Specific conductivity, $\Omega^{-1} \cdot cm^{-1}$	E_A, eV
MW-NTATO	$3.0 \cdot 10^{-11}$	0.31
MW-NTATO/Cu_xO-10	$2.5 \cdot 10^{-12}$	0.43
MW-NTATO/Cu_xO-30	$3.2 \cdot 10^{-13}$	0.45
MW-NTATO/Cu_xO-60	$4.3 \cdot 10^{-14}$	0.51

superposition of lines from defects of the C· type observed in the initial structures, and from O_2^- radicals ($g_1 = 2.029$, $g_2 = 2.009$, $g_3 = 2.003$). The appearance of O_2^- radicals can be explained by oxygen adsorption on oxygen vacancies on TiO_2 surface and, possibly, on the surface of copper oxide nanoparticles, followed by electrons capture from the conduction band. This can lead to a limitation of electron transport and, accordingly, to the conductivity decreasing in MW-NTATO/Cu_xO nanocomposites compared to the initial MW-NTATO structures. With the number of copper oxide deposition cycles increasing, the intensity of the line from Cu^{2+} ions increases. Besides, the intensity of the EPR signal from O_2^- radicals increases, which can be explained by these radicals formation not only on the surface of titanium dioxide, but also on the surface of copper nanoparticles.

Let us proceed to the discussion of the electrophysical properties of the obtained structures. The method of measuring the thermoEMF sign was used to determine the type of conductivity in the structures under study. It was found that all samples have n-type conductivity, which agrees with the literature data for undoped TiO_2. The temperature dependences of the conductivity of the initial MW-NTATO sample and samples modified with Cu_xO nanoparticles are shown in Fig. 6. The structures shown schematically in the insert in Fig. 6 were used to measure the conductivity. The lower electrode was a titanium substrate, on which NTATO samples were directly formed. The upper electrode 3×4 mm was also made of the substrate material and was tightly pressed from above to the NTATO layer. As can be seen from Fig. 6, the temperature dependences of the conductivity are linear in the $\ln(\sigma)$ coordinates from $1000/T$. This means that they can be described by activation dependence:

$$\sigma = \sigma_0 e^{\frac{-E_A}{kT}},$$

where σ_0 — pre-exponential factor weakly dependent on temperature, k — Boltzmann constant, E_A — activation energy.

The Table lists the values of the specific conductivity of MW-NTATO samples measured at temperature of 300 K, as well as the values of activation energy obtained as a result of the approximation of the temperature dependences of the conductivity, depending on the number of copper oxide deposition cycles. It can be seen that the modification of nanotube arrays with Cu_xO particles leads to a significant decrease in the conductivity of the entire structure. For samples with the maximum number of treatment cycles the conductivity decreases by 3 orders of magnitude compared to the initial MW-NTATO samples. It was also found that when Cu_xO is added to the structure, in addition to conductivity decreasing, there is a gradual change in the activation energy, which increases from 0.31 eV for the initial MW-NTATO sample to 0.51 eV for the MW-NTATO/Cu_xO-60 sample.

For a better understanding of the observed effect of the conductivity decreasing of the MC-NTATO/Cu_xO nanocomposites, their current-voltage characteristics (CVCs) were studied. Fig. 7, *a* shows the CVC of the initial MW-NTATO sample, and Fig. 7, *b* — for the MS-NTATO/Cu_xO-60. It can be seen from the Figures that the CVC is symmetrical and non-linear. The CVC nonlinearity is probably associated with the formation of a Schottky barrier at the contact Ti/TiO_2 [23]. The symmetry of the dependence obtained indicates that similar barriers are formed both on the lower and upper electrodes.

Analyzing the above data, we can conclude that the observed significant decrease in the conductivity of MW-NTATO/Cu_xO nanocomposites can be associated with the formation of $p-n$ heterojunction CuO/TiO_2. It can be assumed that this CuO/TiO_2 heterojunction is formed near the top contact as a result of the deposition of CuO particles on the upper layer of TiO_2 nanotubes, as a result of which a structure with $p-n$-transition $Ti/CuO/TiO_2/Ti$ can be formed. However, in this case CVC should have a pronounced diode character [24]. In our case, even for the MW-NTATO/Cu_xO-60 structure with the maximum number of copper treatment cycles (Fig. 7, *b*) the CVC is symmetrical, as is in the case of the original sample. The more linear shape of CVC for the MW-NTATO/Cu_xO-60

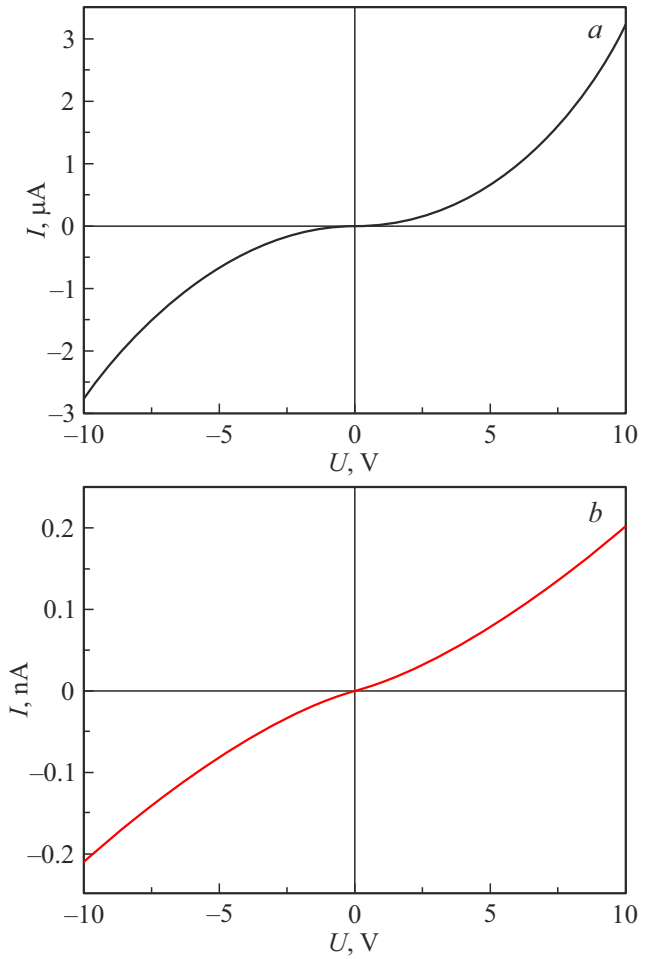

Figure 7. CVCs of the initial MW-NTATO (a) sample and the MW-NTATO/Cu_xO-60 (b) nanocomposite.

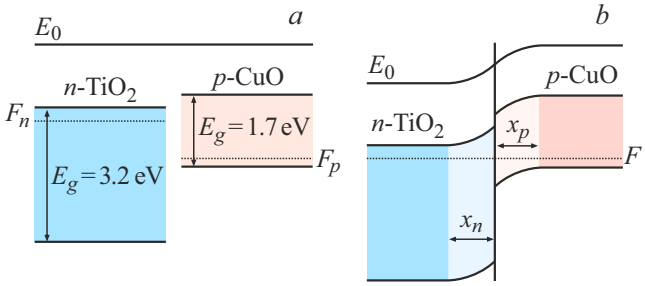

Figure 8. Energy band diagram of TiO_2 and CuO before contact (a), after contact and equilibrium (b).

samples compared to the initial structures is apparently due to a significant increase in the resistance of the titanium dioxide nanotubes themselves, as a result of which the contact resistance at the Ti/TiO_2 interfaces has a smaller effect on the transport of charge carriers in the structure.

Thus, the obtained experimental data indicate that the conductivity decreasing of the MW-NTATO/Cu_xO nanocomposites compared to the initial MW-NTATO is associated with the formation of p-n-heterojunctions on the surface of titanium dioxide nanotubes. To better understand the mechanism of the heterojunctions effect on the structure conductivity, let us consider their energy diagram. Fig. 8, a schematically shows the energy band diagram of TiO_2 and CuO before their contact. The positions of the edges of the energy bands relative to the vacuum level (E_0) are taken from the paper [16].

When two materials of different conductivity types come into contact, electrons diffuse from the n-region to the p-region, and holes diffuse from the p-region to the n-region. Due to the diffusion processes, as well as recombination with the main charge carriers, near the transition the free charge carrier-depletion regions are formed with width of x_n and x_p (Fig. 8, b). If the width of the depleted regions becomes comparable with the thickness of the walls of nanotubes, then the conductivity of such structure in the direction perpendicular to Ti substrate should decrease significantly, which is observed in the experiment. Note that charge transfer in samples modified with copper oxide still proceeds along TiO_2 nanotubes with n-type conductivity. The charge carriers in this case do not overcome the $p-n$-junction, but move along the walls of the nanotubes. The presence of $p-n$-junction affects the concentration of free carriers in nanotubes only. Therefore, CVC of such structure has a symmetrical, but not rectifying form typical for $p-n$-junction. Besides, defects can contribute to the decrease in the conductivity of TiO_2 (n-type) nanotubes. Oxygen molecules are adsorbed on the surface of the samples, followed by the capture of electrons from the conduction band, which leads to the formation of O_2^- radicals detected by the EPR method (see above) and a decrease in the electron concentration in the conduction band. The results obtained provide the key to a better understanding of the electronic processes and mechanisms that determine the change in photocatalytic and sensory properties in such structures.

Conclusion

Thus, arrays of anodic titanium oxide nanotubes were synthesized in this paper, nanocomposites with copper oxide nanoparticles were formed on their basis, they were deposited using the successive ion layer absorption and reaction (SILAR) method, and their detailed study was performed using a set of methods, including microscopy, optical and EPR spectroscopy, electrophysical methods. The resulting wide-band-gap samples are characterized by absorption in the visible region of the spectrum due to the presence of defects, which is important for practical applications, for example, in photocatalysis, since UV sources are not required. The states of defects were studied using EPR spectroscopy. It was established that the main type of paramagnetic sites in nanocomposites are copper ions (Cu^{2+}) and oxygen radical anions (O_2^-), the number of which increases with copper oxide content

increasing in composites. Using the EPR method it was found that copper oxide nanoparticles are present in the studied samples in the form of the CuO phase. The study of the electrophysical properties showed that the structure conductivity decreases by several orders of magnitude with increase in the number of copper oxide deposition cycles. A model is proposed to explain the conductivity decreasing, which assumes the formation of TiO_2/CuO $p-n$-heterojunctions and oxygen chemisorption in the form of O_2^- radicals on surface of the samples, which leads to the formation of charge carriers-depletion layers. For the first time, the effect of the number of copper oxide deposition cycles on the conductivity and defect concentration in TiO_2/Cu_xO nanocomposites is demonstrated in this paper.

Funding

This study was supported by grant No. 21-19-00494 from the Russian Science Foundation (https://rscf.ru/project/21-19-00494/).

Conflict of interest

The authors declare that they have no conflict of interest.

References

[1] M. Zubair, H. Kim, A. Razzaq, C.A. Grimes, S.-I. In. J. CO_2 Util., **26**, 70 (2018).
[2] J. Xiong, M. Zhang, M. Lu, K. Zhao, C. Han, G. Cheng, Z. Wen. Chinese Chem. Lett., **33**, 1313 (2022).
[3] C.A. Grimes, G.K. Mor. TiO_2 *Nanotube Arrays* (Springer US, Boston, MA, 2009)
[4] Z. Liu, X. Zhang, S. Nishimoto, T. Murakami, A. Fujishima. Environ. Sci. Technol., **42**, 8547 (2008).
[5] J. Low, S. Qiu, D. Xu, C. Jiang, B. Cheng. Appl. Surf. Sci., **434**, 423 (2018).
[6] O.K. Varghese, M. Paulose, T.J. LaTempa, C.A. Grimes. Nano Lett., **9**, 731 (2009).
[7] T. Savchuk, I. Gavrilin, E. Konstantinova, A. Dronov, R. Volkov, N. Borgardt, T. Maniecki, S. Gavrilov, V. Zaitsev. Nanotechnology, **33**, 55706 (2022).
[8] S. Rehman, R. Ullah, A.M. Butt, N.D. Gohar, J. Hazard. Mater., **170**, 560 (2009).
[9] E.A. Konstantinova, A.A. Minnekhanov, A.I. Kokorin, T.V. Sviridova, D.V. Sviridov. J. Phys. Chem. C, **122** (18), 10248 (2018).
[10] E.A. Konstantinova, E.V. Kytina, V.B. Zaitsev, M.N. Martyshov, T.P. Savchuk, M.F. Kamaleev. Russ. J. Phys. Chem. B, **16** (4), 797 (2022).
[11] P. Ravi, V. Navakoteswara Rao, M.V. Shankar, M. Sathish. Int. J. Hydrogen Energy, **45**, 7517 (2020).
[12] M.M. Jasim, O. A.A. Dakhil, E.H. Hussein, H.I. Abdullah. J. Mater. Sci. Mater. Electron., **31**, 10707 (2020). DOI: 10.1007/s10854-020-03620-3
[13] Y. Zhao, J. Chen, W. Cai, Y. Bu, Q. Huang, T. Tao, J. Lu. Chem. Phys. Lett., **725**, 66 (2019).
[14] I. Nakamura, N. Negishi, S. Kutsuna, T. Ihara, S. Sugihara, K. Takeuchi. J. Mol. Catal. A Chem., **161**, 205 (2000).
[15] H. Liu, Y. Wang, G. Liu, Y. Ren, N. Zhang, G. Wang, T. Li. Acta Metall. Sin. (English Lett.), **27**, 149 (2014).
[16] R. Marschall. Adv. Funct. Mater. **24**, 2421 (2014).
[17] T. Ohsaka, F. Izumi, Y. Fujiki. J. Raman Spectrosc., **7**, 321 (1978).
[18] L. Debbichi, M.C. Marco de Lucas, J.F. Pierson, P. Krüger. J. Phys. Chem. C, **116**, 10232 (2012).
[19] A.V. Shabalina, A.G. Golubovskaya, E.D. Fakhrutdinova, S.A. Kulinich, O.V. Vodyankina, V.A. Svetlichyi. Nanomaterials , **12**, 4101 (2022). https://doi.org/10.3390/nano12224101
[20] U.I. Gaya. Europ. J. Chem., **2** (2), 163 (2011).
[21] K. Byung-Hyun, P. Mina, K. Gyubong, K. Hermansson, P. Broqvist, C. Heon-Jin, L. Kwang-Ryeol. J. Phys. Chem. C, **122** (27), 15297 (2018).
[22] A.I. Kokorin. In *Chemical Physics of Nanostructured Semiconductors* (CRC Press, London, 2003), p. 203–261.
[23] P.A. Mini, A. Sherine, K.T. Shalumon, A. Balakrishnan, S.V. Nair, K.R.V. Subramanian. Appl. Phys. A., **108**, 393 (2012).
[24] O. Alev, E. Şennik, Z.Z. Öztürk. J. Alloys Compd., **749**, 221 (2018). DOI: 10.1016/j.jallcom.2018.03.268